Free vibration analysis of variable stiffness composite laminated beams and plates by novel hierarchical differential quadrature finite elements

Composite Structures 274 (2021) 114364

Contents lists available at ScienceDirect

Composite Structures

journal homepage: www.elsevier.com/locate/compstruct

Free vibration analysis of variable stiffness composite laminated beams and plates by novel hierarchical differential quadrature finite elements

Yang Yan [a,*], Bo Liu [a], Yufeng Xing [a], Erasmo Carrera [b,c], Alfonso Pagani [b]

[a] School of Aeronautic Science and Engineering, Beihang University, Xueyuan Road 37, 100191 Beijing, China
[b] MUL2, Department of Mechanical and Aerospace Engineering, Politecnico di Torino, Corso Duca degli Abruzzi 24, 10129 Torino, Italy
[c] Department of Mechanical Engineering, College of Engineering, Prince Mohammad Bin Fahd University P.O. Box 1664, Al Khobar 31952, Saudi Arabia

ARTICLE INFO

Keywords:
Variable-angle-tow composites
Carrera Unified Formulation
Free vibration
Differential quadrature finite element method
Improved hierarchical Legendre expansions

ABSTRACT

The present work deals with the free vibration behavior of the variable stiffness composite laminates (VSCLs) featured by spatially varying fibre orientation angles via novel quasi-three-dimensional solutions. The Carrera Unified Formulation (CUF) is employed to construct such novel models, where cross-section kinematics are described with the improved hierarchical Legendre expansion (IHLE) of primary mechanical variables. The proposed expansions not only maintain the hierarchical properties of the HLE model but also become less sensitive to the numbering sequence of expansion terms. As a result of these enhanced kinematics, Equivalent Single Layer (ESL) and Layer-Wise (LW) models can be formulated more robustly. The weak form differential quadrature finite element method (DQFEM) is employed to solve the governing equations derived by the principle of virtual displacements. Based on CUF-based DQFEM, even a single beam element is sufficient to tackle many complex issues with high accuracy. Compact VSCL beams and plates with various fibre paths, boundary conditions, lamination schemes, and thickness-to-width ratios have been studied in several numerical examples. The proposed method's accuracy and effectiveness are validated by comparing results to published data.

1. Introduction

Composite materials as an alternative to their metallic counterparts have been extensively used in aircraft structures, such as wings or rotor blades. Classical fibre-reinforced composites are made of straight fibres and a polymer matrix. Structural performance can be optimized through the adjustment of fibre orientation angles and stacking sequences. However, in the practical lay-up design, fibre orientation angles vary between four different values, i.e., $0^0, 45^0, -45^0, 90^0$ [1]. Such a limitation precludes the considerable utilization of the anisotropic features of composite materials. Besides, straight-fibre-based laminates are only endowed with a constant in-plane stiffness within the layer. For this reason, they are also referred to as Constant Stiffness Composite Laminates (CSCLs). In contrast to CSCLs, the notion of Variable Stiffness Composite Laminates (VSCLs) has been proposed to achieve a better tailoring capability of laminated composites. In fact, there are many approaches to modify the in-plane stiffness locally, including the adjustment of fibre volume fraction [2,3], the alteration of thickness by terminating individual plies [4,5], the attachment of stiffeners to the laminate [6,7] and the placement of curvilinear fibres [8,9]. The present paper focuses on the variable fibre orientation angle category.

Hyer and Lee [10] originally introduced the use of the curvilinear fibre format for enhanced structural performance. They assumed that fibre orientation angles varied in a region-wise manner. By employing sensitivity analyses and gradient-search techniques, the optimal angle in each region can be determined in terms of the maximum bucking load. The results indicated that improved buckling capability and tensile performance can be obtained by introducing the curvilinear fibre concept. However, such an arrangement of fibres is hard to be produced since manufacturing techniques, e.g., Automatic Fibre Placement (AFP), can only produce continuous fibre courses. Gürdal and Olmedo [11] utilized a linear function to describe the variation of orientation angles so that closed-form solutions can be obtained for some special boundary conditions. Following the linear angle variation path described previously, Tatting and Gürdal [12,13] developed a lamination definition tool capable of reading the information hidden in curvilinear fibres as easily as straight fibres and integrating it with finite

* Corresponding author.
E-mail addresses: yanyang864914630@126.com (Y. Yan), liubo68@buaa.edu.cn (B. Liu), xingyf@buaa.edu.cn (Y. Xing), erasmo.carrera@polito.it (E. Carrera), alfonso.pagani@polito.it (A. Pagani).

https://doi.org/10.1016/j.compstruct.2021.114364
Received 12 April 2021; Revised 2 July 2021; Accepted 12 July 2021
Available online 22 July 2021

element models and a stacking sequence optimization program, i.e., Optimization of Laminates using Genetic Algorithms (OLGA) for the buckling design of VSCLs. Besides, testing specimens manufactured by a tow-placement machine have shown their enhanced performance against buckling and failure loads. Wu et al. [14] also performed an experimental study to investigate the nonlinear response of VSCLs when mechanical and thermal prestresses are taken into account. As a matter of fact, fibre orientation angles can be defined by a nonlinear function as well. Wu et al. [15] used Lagrangian polynomials to represent the variation of fibre orientation angles in a more generic fashion, and the results showed that such a kind of polynomials could improve the buckling load than linear ones. Alhajahmad et al. [16] employed Lobatto-Legendre polynomials to define the angle of steered fibres, and the improvement in load-carrying capacity can be likewise achieved. It should be pointed out that the AFP process is subject to a set of manufacturing constraints. For instance, if the fibre steering radius is shorter than a critical threshold, i.e., the minimum turning radius, the inner edges of tows tend to be wrinkle, causing a loss of structural strength. Thus, whether the non-linear definition of fibre orientation angles meets such a strict requirement merits special consideration, although no experimental investigation involving this type of VSCLs has been published.

The preceding review of the literature mainly concentrates on the static behavior of VSCLs. Vibration-based issues are presented hereinafter. Akhavan and Ribeiro [17] utilized the third-order shear deformation theory (TSDT) for the vibration analysis of the VSCL panels with linearly varying fibre orientation angles. They found that, in comparison to thick VSCL ones, the natural frequencies of thin VSCL plates are more sensitive to the fibre path. The B-spline function was adopted to describe the variation of fibre orientation angles by Honda and Narita [18]. This work showed that mode shapes has a tight connection with fibre shapes. Akbarzadeh et al. [19] extended TSDT to investigate the vibratory characteristics of the VSCLs bonded with magnetostrictive layers. The influence of the hygrothermal environment on the free vibration characteristics of the VSCL plates with cut-outs was investigated by Venkatachari et al. [20] using the first-order shear deformation theory. From their research, it can be observed that the fibre orientation angles at the centre and edge play a more important role in the maximum/minimum values of natural frequencies than lay-up configurations. The same shear deformation theory was also applied to the VSCLs with elastically restrained edges [21], VSCL skew plates [22], VSCL elliptical plates [23] and the stiffened VSCL plates subjected to in-plane loads [24]. Houmat [25] carried out 3D free vibration analyses of VSCLs via *p*-FEM and pointed out that a 3D model is demanded for the VSCL plates with large thickness-to-width ratios and anti-symmetric stacking sequences. The same conclusion was also drawn in Yazdani and Ribeiro [26], where a Layer-wise (LW) modeling approach, was chosen.

The FEM provides an outstanding computational framework for analyzing complex aircraft structures. However, the 3D FE model is not particularly recommended for computing composite structures because the aspect ratio of the solid element is directly proportional to the layer thickness. On the other hand, 1D and 2D elements based on beam and plate(shell) theories are more efficient in terms of degrees of freedom, considering simplified kinematic assumptions made over the cross-section or across the thickness of structures. The Carrera Unified Formulation (CUF), proposed by Carrera et al. [27] is a hierarchical theory that enables the automatic and straightforward development of beam, plate, and shell theories, demonstrating its 3D-like accuracy while requiring less computational resources. CUF was initially developed for plates and shells, hereafter called 2D CUF and subsequently extended for beams, hereafter referred to as 1D CUF. Within the framework of 1D CUF, the Equivalent Single Layer (ESL) and LW assumptions of cross-section kinematics can be obtained in a straightforward and systematic manner by the correct employment of the expansion function of 1D unknown variables, e.g., displacement [28] or stress [29] components. So far, four kinds of expansion modes have been developed based on Taylor series, Lagrange polynomials, Chebyshev polynomials and hierarchical Legendre polynomials, leading to the theories of so-called CUF-Taylor expansion (CUF-TE) [30], -Lagrange expansion (LE) [31,32], -Chebyshev expansion (CE) [33], and -hierarchical Legendre expansion (HLE) [34,35]. Viglietti et al. [36,37] employed the proposed 1D refined model to analyze the free vibration of the VSCLs ranging from a simple plate-like configuration to a complex wing structure with a NACA profile, where ESL models are constructed with TE and LW ones are generated by LE. The same procedure has been used by Pagani et al. [38,39] to show how manufacturing flaws, e.g., fibre misalignments affect the buckling and failure behaviors of VSCLs. There is currently no literature describing the use of HLE for the corresponding analysis. As a matter of fact, the CUF-HLE model combines the advantages of the hierarchy of the higher-order terms in the CUF-TE model and the local description of the cross-section kinematics in the CUF-LE model, thus providing an additional option for the development of both the ESL and LW models. However, the correspondence of the shared sides between adjacent expansion domains cannot be satisfied naturally in the HLE-based LW model because the degrees of freedom on the border of the cross-section specified by HLE do not have a clear physical meaning. By virtue of the guideline for the formulation of 2D and 3D elements in the differential quadrature hierarchical finite element method (DQHFEM) proposed by Liu et al. [40,41], the present paper tends to develop a novel type of 1D CUF models called the improved hierarchical Legendre expansion (IHLE), which introduces the Lagrange interpolation basis on the edge of expansion domains while keeping the hierarchical Legendre interpolation basis on the inside. This novel expansion not only allows the matrix assembly of cross-section subdomains to be implemented more conveniently, as the manner in LE, but also retains the hierarchical properties of HLE.

Besides, in the majority of the literature concerning 1D CUF, FEM has been emerged as a powerful tool in the handling of arbitrary geometries and loading conditions. The achieved accuracy and convergence rate scale with the type of the pre-selected element. Carrera et al. [42] pointed out that low-order beam elements, such as two- or three-node beam elements, exhibit various degrees of locking. For this reason, the development of high-order methods deserves much attention since as rapid convergence can be envisaged in conjunction with a locking-free occurrence. Alternatively, the differential quadrature finite element method (DQFEM) [43,44] is one of a group of weak-formulation-based approaches and allows for a unified formulation of the element from lower to higher order. In contrast to the standard FEM, DQFEM performs integration via the Gauss–Lobatto rule prior to dealing with the derivative of a function. Due to the coincidence of the integration point and element node, the high-order approximation of the derivatives at arbitrary integration points becomes possible by using the DQ rule without the construction of the shape function. Furthermore, such a coincidence can be regarded as a reduced integration scheme, accounting for the mechanism of the locking alleviation indeed.

The current work makes an endeavour to develop a novel beam model combined with DQFEM to solve the free vibration problem of VSCLs. The rest of this paper is organized as follows. Initially, the mathematical description of the fibre orientation angle and material stiffness matrix of VSCLs is outlined Section 2; then, the CUF kinematic field is explained in Section 3, where insights about the relationship between HLE and IHLE are provided; the introduction of DQFEM, the derivation of the fundamental nucleus and its implementation in ESL and LW manners are presented in Section 4; the potential of the proposed approach is shown in Section 5 via the consideration of VSCL beams and plates; finally, the main conclusions are drawn in Section 6.

2. Variable stiffness composite laminates

Consider a typical VSCL structure composed of N_l layers in the Cartesian reference system, whose geometric size is characterized by the length L, the width W, and the height H. Assume that each layer is made of the same material but with different fibre orientation angles. As distinguished from conventional straight-fibre-based laminates, each lamina in a VSCL structure can be manufactured by steering the fibre along an arbitrary curvilinear path, as shown in Fig. 1. The present paper employs a x-coordinate-dependent linear formulation to define the variation of the fibre orientation angle $\theta(x)$ in the kth layer, which is given by

$$\theta^k(x) = T_0^k + 2\frac{(T_1^k - T_0^k)}{W}|x| \tag{1}$$

where T_0 and T_1 represent the angles at the center $x = 0$ and the edge $x = |W/2|$ of the structure. The superscript T denotes the transposition operator. $\langle T_0/T_1\rangle$ is used to characterize the lamination angle in a single VSCL ply. For the sake of convenience, the notation k will be omitted in the majority of the formulation derivation below.

For small displacements, the relation between strain $\boldsymbol{\varepsilon} = \left[\varepsilon_{yy}\ \varepsilon_{xx}\ \varepsilon_{zz}\ \varepsilon_{xz}\ \varepsilon_{yz}\ \varepsilon_{xy}\right]^{\mathrm{T}}$ and displacement $\mathbf{u} = \left[u_x, u_y, u_z\right]^{\mathrm{T}}$ can be prescribed through the linear differential operator matrix as:

$$\boldsymbol{\varepsilon} = \mathbf{D}\mathbf{u} \tag{2}$$

where

$$\mathbf{D} = \begin{bmatrix} 0 & \frac{\partial}{\partial y} & 0 \\ \frac{\partial}{\partial x} & 0 & 0 \\ 0 & 0 & \frac{\partial}{\partial z} \\ \frac{\partial}{\partial z} & 0 & \frac{\partial}{\partial x} \\ 0 & \frac{\partial}{\partial z} & \frac{\partial}{\partial y} \\ \frac{\partial}{\partial y} & \frac{\partial}{\partial x} & 0 \end{bmatrix} \tag{3}$$

In addition, Hooke's law can now be exploited to give stress components $\boldsymbol{\sigma} = \left[\sigma_{yy}\ \sigma_{xx}\ \sigma_{zz}\ \sigma_{xz}\ \sigma_{yz}\ \sigma_{xy}\right]^{\mathrm{T}}$ as:

$$\begin{aligned} \boldsymbol{\sigma} &= \tilde{\mathbf{C}}\boldsymbol{\varepsilon}\boldsymbol{\varepsilon} \\ \tilde{\mathbf{C}}(x) &= \mathbf{T}(x)\mathbf{C}_m\mathbf{T}^{\mathrm{T}}(x) \end{aligned} \tag{4}$$

where $\tilde{\mathbf{C}}_{\mathbf{m}}$ and $\tilde{\mathbf{C}}(x)$ are the material stiffness matrices specified in material coordinate $[2, 3, 1]$ and Cartesian $[x, y, z]$ systems, respectively; and $\mathbf{T}$ is the rotation matrix. For the sake of brevity, the components of $\tilde{\mathbf{C}}_{\mathbf{m}}$ and $\mathbf{T}$ are not provided here but can be found in [45]. Moreover, since $\tilde{\mathbf{C}}(x)$ changes point by point in VSCL structures, managing this adjustment is more tricky, as detailed in the Section 4.

3. Carrera Unified Formulation (CUF)

Although the variation of the fibre orientation angle in VSCL structures is dependent on the x-coordinate, it is not an impediment to the effectiveness of CUF, which has been proven applicable over a wide range of structural geometries and material properties [27]. The core idea of 1D CUF is to express the 3D displacement vector as the cross-section expansion of 1D generalized displacements along the y-direction, the explicit form of which can be written as:

$$\mathbf{u}(x, y, z; t) = F_\tau(x, z)\mathbf{u}_\tau(y; t) \quad \tau = 1, \ldots, M \tag{5}$$

where $\mathbf{u}_\tau(y; t)$ is a generalized displacement vector function; a repeated index τ, according to the Einstein convention, stands for summation; and $F_\tau(\xi, \eta)$ represents the expansion function. The high-fidelity simulation of cross-section deformation counts on the type of expansion functions (TE, LE, CE, HLE) and the number of expansion terms.

3.1. Hierarchical Legendre expansion

Inspired by the work done by Babuska et al. [46], who used the 2D set of Legendre polynomials to construct the shape function of plane-type elements, Carrera et al. [34] proposed a new beam model, which characterizes cross-section deformation via such kind of polynomials. They can be classified into three groups: vertex modes, side modes, and internal modes. Their expressions are defined in terms of natural coordinates (ξ, η), as illustrated bellow.

Vertex modes: they are used to describe nodal deformation values over the quadrilateral sub-domain.

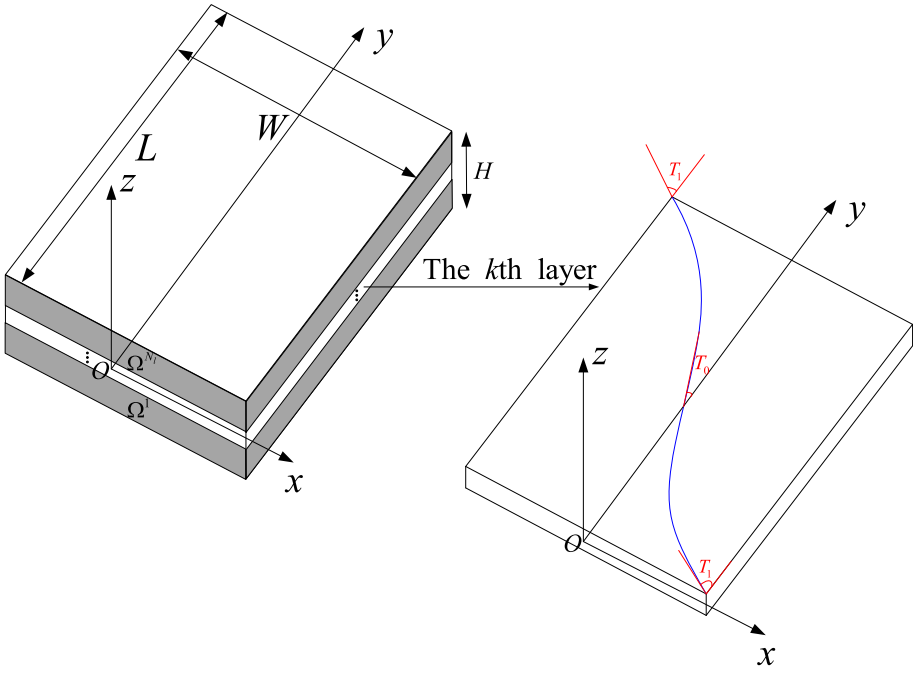

Fig. 1. Coordinate system for a tow-steered composite laminate.

$$F_\tau = \frac{1}{4}(1+\xi\xi_\tau)(1+\eta\eta_\tau); \qquad \tau = 1,2,3,4,\ldots \tag{6}$$

where ξ_τ and η_τ are the coordinates of four vertexes in the natural coordinate system. ξ and η vary within the range of [-1, +1].

Side modes: they are used to represent the deformation of the edge over the quadrilateral sub-domain.

$$\begin{aligned}
&F_\tau = \tfrac{1}{2}(1-\eta)\phi_{j_1}(\xi); && j_1 \geqslant 2; && \tau = 5,9,13,18,\ldots\\
&F_\tau = \tfrac{1}{2}(1+\xi)\phi_{j_2}(\eta); && j_2 \geqslant 2; && \tau = 6,10,14,19,\ldots\\
&F_\tau = \tfrac{1}{2}(1+\eta)\phi_{j_3}(\xi); && j_3 \geqslant 2; && \tau = 7,11,15,20,\ldots\\
&F_\tau = \tfrac{1}{2}(1-\xi)\phi_{j_4}(\eta); && j_4 \geqslant 2; && \tau = 8,12,16,21,\ldots
\end{aligned} \tag{7}$$

where $j_i; \quad i = 1,2,3,4$ stands for the order of the expansion function at the ith edge; and ϕ_{j_i} is the integrated Legendre polynomial, the detailed description of which can be seen in [34]. Note that the expansion order of each side mode may vary individually. Because two orthogonal dimensions over the cross-section have geometrical resemblance, the order of ϕ_{j_i} on each side is supposed to be equal for the beam-like structure. In the case of the plate-like structure, the width and thickness dimensions are not in the same order of magnitude. In terms of modeling, the order of ϕ_{j_i} in the thickness direction should be certainly different than that in the width direction. As a result, the enhanced capability of side-dependent kinematics can be used to model beam and plate-like structures in an automatic manner.

Internal modes: they are used to depict the deformation inside the quadrilateral sub-domain and disappear at nodes and edges.

$$\begin{aligned}
&F_\tau = \phi_{j_m}(\xi)\phi_{k_n}(\eta); \qquad j_m, k_n \geqslant 2; \qquad m,n = 1,2,3,4;\\
&\tau = 17,22,23,28,29,30\ldots
\end{aligned} \tag{8}$$

Fig. 2 plots the mode shapes of HLE from order 1 to 4 for the beam case. HLE defines cross-section kinematics in the isoparametric reference system. As a result, the LW model can be built by locally refining kinametic terms in each of reinforced layers, as is the way in LE. Moreover, the kinematics defined by HLE are hierarchical, meaning that the polynomial order can be increased by adding higher-order functions to the existing set (as is done in the TE and CE). This characteristic makes it possible to realize the ESL model. Therefore, HLE combines the benefits of the TE, CE, and HLE and is frequently used in CUF analyses.

The figure also shows that the side modes for the third-order expansion do not have the same axisymmetric shape as those for the second-order expansion but they do have a centrosymmetric form. Because of this feature, the C^0 continuity of the displacements at layer interfaces cannot be guaranteed if the nodal numbering scheme is not designed discreetly. As an illustration, consider a two-layer laminate with each layer modeled by the four-order expansion. The global nodal numbering scheme and deformation pattern per layer are shown in Fig. 3. As for the individual layer, there are four kinds of nodal numbering schemes, beginning from four separate vertices. Here we consider two possible cases of local nodal numbering schemes, i.e., Case I and II (Fig. 3). In Case I, both bottom and top layers have the identical nodal numbering scheme, which starts at the bottom left corner and travels anticlockwise around the layer's edge until ending inward. In Case II, we replace an existing nodal numbering scheme for the bottom layer, this time starting from the bottom right corner. The displacement discontinuous phenomena appears at intra-layer interfaces as a result of such a minor change. In other words, the outcomes of the HLE model are highly dependent on each layer's nodal numbering scheme.

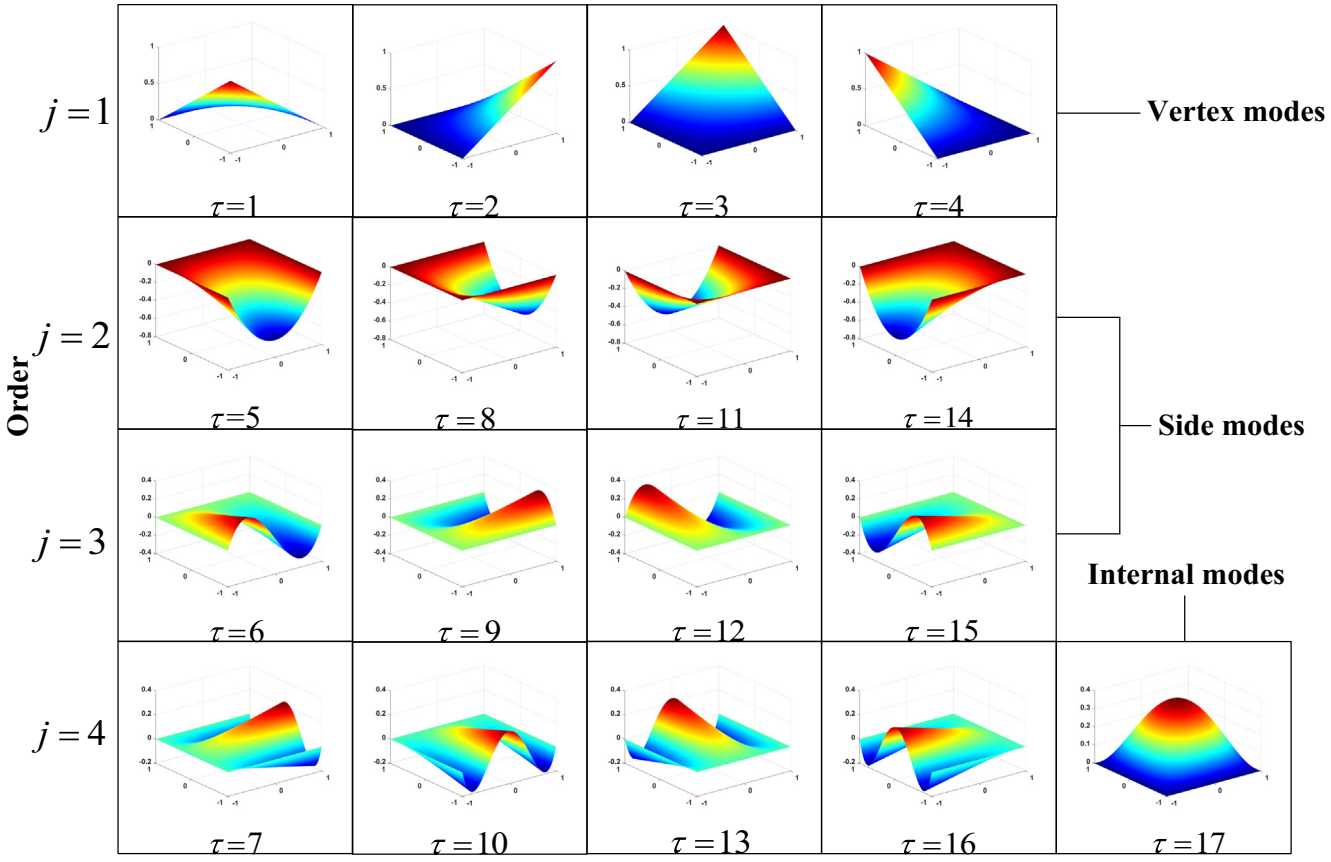

Fig. 2. Hierarchical Legendre polynomials with the order from 1st to 4th.

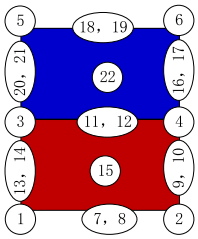

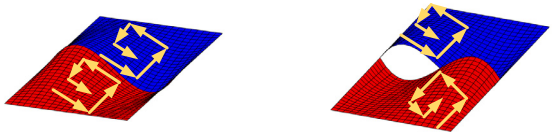

Case I
Bottom Layer:
[1,2,4,3,7,8,9,10,12,11,14,13,15].
Top Layer:
[3,4,6,5,12,11,16,17,19,18,21,20,22].

Case II
Bottom Layer:
[2,4,3,1,9,10,12,11,14,13,7,8,15].
Top Layer:
[3,4,6,5,12,11,16,17,19,18,21,20,22].

Fig. 3. Global nodal numbering scheme and the deformations caused by Case I and II.

3.2. Improved hierarchical Legendre expansion

A straightforward approach is to convert the non-interpolative bases related to hierarchical side modes into Lagrange-type nodal bases. Such an operation leads to the improved hierarchical Legendre expansion (IHLE), which represents one novelty of the present work.

Fig. 4 specifies the transformed nodes related to the kth layer. It should be added that the total number of transformed nodes should be equal to that of the expansion terms relative to vertex and side modes. As a result of the mathematical issue, the nodal collocation strategy is such that non-equispaced nodes, namely, Gauss–Lobatto nodes, are selected for each line so that the serious oscillation phenomenon with a growing number of nodes, referred to as Runge's phenomenon, can be weakened to some extent. If $\mathbf{u}_\tau^{\mathrm{g}}(y;t) = \left[u_{x\tau}^{\mathrm{g}}, u_{y\tau}^{\mathrm{g}}, u_{z\tau}^{\mathrm{g}}\right]^{\mathrm{T}}$ is the displacement vector of the τth Gauss–Lobatto node (ξ_τ, η_τ). Its value can be computed using the following equation:

$$\boldsymbol{U}_\tau^{\mathrm{g}} = \mathbf{V}\boldsymbol{U}_\tau \tag{9}$$

where $\boldsymbol{U}_\tau^{\mathrm{g}}$ is a vector, which is constructed from $\mathbf{u}_\tau^{\mathrm{g}}(y;t)$; and $\mathbf{V}$ is defined in a similar way; $\boldsymbol{U}_\tau$ is the vectorization representation of $\mathbf{u}_\tau(y;t)$. These new terms are expressed as follows:

$$\begin{aligned}
\boldsymbol{U}_\tau^{\mathrm{g}} &= \left[u_{x1}^{\mathrm{g}}, \ldots, u_{z1}^{\mathrm{g}}, \ldots, u_{x\tau}^{\mathrm{g}}, \ldots, u_{z\tau}^{\mathrm{g}}, \ldots, u_{xN}^{\mathrm{g}}, \ldots, u_{zN}^{\mathrm{g}}\right]^{\mathrm{T}} \\
\mathbf{V} &= \begin{bmatrix}
F_1(\xi_1,\eta_1) & \cdots & F_\tau(\xi_1,\eta_1) & \cdots & F_N(\xi_1,\eta_1) \\
\cdots & \cdots & \cdots & \cdots & \cdots \\
F_1(\xi_\tau,\eta_\tau) & \cdots & F_\tau(\xi_\tau,\eta_\tau) & \cdots & F_N(\xi_\tau,\eta_\tau) \\
\cdots & \cdots & \cdots & \cdots & \cdots \\
F_1(\xi_N,\eta_N) & \cdots & F_\tau(\xi_N,\eta_N) & \cdots & F_N(\xi_N,\eta_N)
\end{bmatrix} \otimes \mathbf{I} \\
\boldsymbol{U}_\tau &= \left[u_{x1}, \ldots, u_{z1}, \ldots, u_{x\tau}, \ldots, u_{z\tau}, \ldots, u_{xN}, \ldots, u_{zN}\right]^{\mathrm{T}}
\end{aligned} \tag{10}$$

where $\otimes$ stands for the Kronecker product; $\mathbf{I}$ is the 3×3 identity matrix; and N indicates the total amount of vertex and side modes.

Based on Eq. (9), the local displacement field related to four edges $\mathbf{u}^{\mathrm{fes}}(x,y,z;t)$ in the kth layer can be written as follows:

$$\mathbf{u}^{\mathrm{fes}} = \mathbf{G}\mathbf{V}^{-1}\boldsymbol{U}_\tau^{\mathrm{g}} = L_\tau(\xi,\eta)\mathbf{u}_\tau^{\mathrm{g}}(y;t); \qquad \tau = 1,2,\ldots,N \tag{11}$$

where $\mathbf{G} = [F_1, F_2, \ldots, F_N] \otimes \mathbf{I}$ is the matrix form of the expansion function $F_\tau(\xi,\eta) \quad \tau = 1,2,\ldots,N$; and L_τ means the Lagrange-type nodal base and its component can be computed via $\mathbf{G}\mathbf{V}^{-1}$.

It is worth mentioning Eq. (11) has a shortcoming in terms of calculating the displacement field within the layer. In fact, in view of Fig. 2, internal modes have no effect on the displacement patterns along four edges despite their critical significance in the versatile description of full displacement fields. Such a crucial feature offers the possibility of formulating a novel kinematic field, which states that:

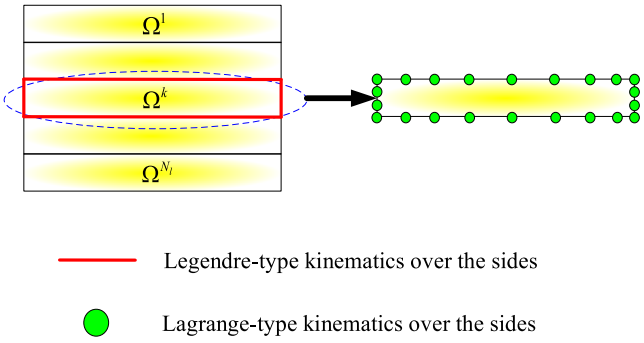

Fig. 4. Transformed nodes of the kth layer.

$$\begin{aligned}
&\mathbf{u} = L_{\tau_1}(\xi,\eta)\mathbf{u}_{\tau_1}^{\mathrm{g}}(y;t) + F_{\tau_2}(\xi,\eta)\mathbf{u}_{\tau_2}(y;t); \quad \tau_1 = 1,2,\ldots,N; \\
&\tau_2 = 1,2,\ldots,M-N; \quad \tau_1 \neq \tau_2 \\
&= \bar{F}(\xi,\eta)\mathbf{u}_\tau(y;t); \quad \tau = 1,2,\ldots,M
\end{aligned} \tag{12}$$

where $\bar{F}(\xi,\eta)$ means the IHLE function, which is a mix of Lagrange and hierarchical Legendre polynomials.

The main advantage of the proposed kinematic formulation is that the C^0 continuity of the displacements at the intra-layer interfaces can be satisfied spontaneously without some special treatment on the nodal numbering scheme, resulting in an increased efficiency in the pre-processing stage. In addition, the Lagrange expansion on edges can be acquired through the transformation method given by Eq. (11), retaining the integrity of the input data of the original HLE model. The transformation efficiency depends on the time consumption of the matrix inversion in Eq. (11).

4. DQFE formulation

Due to its simplicity and broad applicability, the conventional low-order FE formulation is extensively used in mechanistic studies of structures. However, A sufficient number of elements are essential for ensuring the analysis accuracy. As an alternative, the DQFE formulation belongs to a kind of the high-order FE formulation, showing a good compromise between the accuracy and the number of elements. Accordingly, the generalized displacements along the beam axis can be interpolated via the following expression:

$$\mathbf{u}_\tau = N_i(y)\mathbf{u}_{\tau i} \quad i = 1,\ldots,n \tag{13}$$

where $\mathbf{u}_{\tau i}$ refers to the unknown nodal vector; n indicates the number of nodes within the element; and $N_i(y)$ denotes Lagrange interpolating basis functions in the following manner:

$$N_i(\gamma) = \frac{\prod_{j=1}^{n_{\mathrm{elem}}}(\gamma - \gamma_j)}{\prod_{j=1, j\neq i}^{n_{\mathrm{elem}}}(\gamma_i - \gamma_j)} \tag{14}$$

where N_i is defined using the isoparametric coordinate γ. To minimize problematic oscillations in numerical solutions, Gauss–Lobatto collocation points are chosen as the roots of the polynomials with high-order degrees.

It is not easy to express the first-order derivatives of a set of the shape functions in Eq. (14) in an explicit form. The corresponding expressions for the low-order case can be determined term-by-term. On the contrary, it is a tedious work for the high-order counterpart. Alternatively, their explicit expressions at the interpolation point can

be smoothly achieved with the aid of the DQ rule. For example, the first-order derivative of $u_{x\tau}$ at the i^{th} Gauss–Lobatto node reads

$$u_{x\tau_{,y}}\big|_{y=y_i} = A_{ij}u_{x\tau j} \quad i=1,\ldots,n_{\text{elem}} \quad j=1,\ldots,n_{\text{elem}} \tag{15}$$

where A_{ij} represents the weighting coefficients for its first derivative and can be written as

$$\begin{aligned} A_{ij} &= \frac{\phi(\gamma_i)}{\phi(\gamma_j)(\gamma_i-\gamma_j)}; \qquad i=1,2,\ldots,n_{\text{elem}}; \quad j=1,2,\ldots,n_{\text{elem}}; \quad i\neq j \\ A_{ii} &= -\sum_{j=1 j\neq i}^{n} A_{ij}; \qquad i=1,2,\ldots,n_{\text{elem}} \end{aligned} \tag{16}$$

Although the formulation described here is limited to the special point, it serves as the foundation for the implementation of DQFEM, which performs numerical integration via the Gauss–Lobatto rule. Specific details are discussed in the following sub-section.

4.1. DQFEM fundamental nucleus

Based on the CUF-IHLE, the weak-form governing equation for the free vibration problem can be derived via the principle of virtual displacements (PVD), which states that:

$$\delta L_{\text{int}} + \delta L_{\text{ine}} = 0 \tag{17}$$

where δL_{int} means the virtual variation of the strain energy and δL_{ine} is the virtual variation of the inertial work. In detail, δL_{int} takes the following integral form:

$$\delta L_{\text{int}} = \int_L \int_\Omega \delta\boldsymbol{\varepsilon}^{\mathrm{T}}\boldsymbol{\sigma}\mathrm{d}\Omega\mathrm{d}y = \delta\mathbf{u}_{\tau i}\mathbf{K}^{ij\tau s}\mathbf{u}_{sj} \tag{18}$$

and δL_{ine} is given by

$$\delta L_{\text{ine}} = \int_L \int_\Omega \rho\delta\mathbf{u}\ddot{\mathbf{u}}\mathrm{d}\Omega\mathrm{d}y = \delta\mathbf{u}_{\tau i}\mathbf{M}^{ij\tau s}\ddot{\mathbf{u}}_{sj} \tag{19}$$

where ρ is the material density; and $\mathbf{K}^{ij\tau s}$ and $\mathbf{M}^{ij\tau s}$ are 3×3 stiffness and mass matrices denoted to as fundamental nuclei, which are invariant to the cross-section expansion order. Thus various beam theories available can be generated in a unified manner. The mathematical expressions of these matrices yield:

$$\begin{aligned}
K^{\tau sij}_{(11)} &= \left(E^{22}_{\tau_{,x}s_{,x}} + E^{44}_{\tau_{,z}s_{,z}}\right)J_{ij} + E^{26}_{\tau_{,x}s}J_{ij,y} + E^{26}_{\tau s,x}J_{i,yj} + E^{66}_{\tau s}J_{i,yj,y} \\
K^{\tau sij}_{(12)} &= \left(E^{26}_{\tau_{,x}s_{,x}} + E^{45}_{\tau_{,z}s_{,z}}\right)J_{ij} + E^{23}_{\tau_{,x}s}J_{ij,y} + E^{66}_{\tau s,x}J_{i,y}j + E^{36}_{\tau s}J_{i,y}j_{,y} \\
K^{\tau sij}_{(13)} &= \left(E^{12}_{\tau_{,x}s_{,z}} + E^{44}_{\tau_{,z}s_{,x}}\right)J_{ij} + E^{45}_{\tau_{,z}s}J_{ij,y} + E^{16}_{\tau s,z}J_{i,yj} \\
K^{\tau sij}_{(21)} &= \left(E^{26}_{\tau_{,x}s_{,x}} + E^{45}_{\tau_{,z}s_{,z}}\right)J_{ij} + E^{66}_{\tau_{,x}s}J_{ij,y} + E^{23}_{\tau s,x}J_{i,y}j + E^{36}_{\tau s}J_{i,yj,y} \\
K^{\tau sij}_{(22)} &= \left(E^{66}_{\tau_{,x}s_{,x}} + E^{55}_{\tau_{,z}s_{,z}}\right)J_{ij} + E^{36}_{\tau_{,x}}J_{ij,y} + E^{36}_{\tau s,x}J_{i,y}j + E^{33}_{\tau s}J_{i,y}j_{,y} \\
K^{\tau sij}_{(23)} &= \left(E^{16}_{\tau_{,x}s_{,z}} + E^{45}_{\tau_{,z}s_{,x}}\right)J_{ij} + E^{55}_{\tau_{,z}}J_{ij,y} + E^{13}_{\tau s,z}J_{i,yj} \\
K^{\tau sij}_{(31)} &= \left(E^{44}_{\tau_{,x}s_{,z}} + E^{12}_{\tau_{,z}s_{,x}}\right)J_{ij} + E^{16}_{\tau_{,z}s}J_{ij,y} + E^{45}_{\tau s,z}J_{i,yj} \\
K^{\tau sij}_{(32)} &= \left(E^{45}_{\tau_{,x}s_{,z}} + E^{16}_{\tau_{,z}s_{,x}}\right)J_{ij} + E^{13}_{\tau_{,z}s}J_{ij,y} + E^{55}_{\tau s,z}J_{i,yj} \\
K^{\tau sij}_{(33)} &= \left(E^{44}_{\tau_{,x}s_{,x}} + E^{11}_{\tau_{,z}s_{,z}}\right)J_{ij} + E^{45}_{\tau_{,x}s}J_{ij,y} + E^{45}_{\tau s,x}J_{i,yj} + E^{55}_{\tau s}J_{i,yj,y} \\
\mathbf{M}^{\tau\zeta ij} &= E^{\rho}_{\tau_\zeta}J_{ij}\mathbf{I}
\end{aligned} \tag{20}$$

where $E^{\alpha\beta}_{\tau_{,\theta}s_{,\zeta}}$ and $J_{i_{,\zeta}j_{,\zeta}}$ represent the cross-section moment parameter and integrals along the beam axis, which read:

$$\begin{aligned} E^{\alpha\beta}_{\tau_{,\theta}s_{,\zeta}} &= \int_\Omega \tilde{C}_{\alpha\beta}(x)F_{\tau,\theta}(x,z)F_{s,\zeta}(x,z)\mathrm{d}\Omega \\ J_{i_{,\zeta}j_{,\zeta}} &= \int_L N_{i,\zeta}(y)N_{j,\zeta}(y)\mathrm{d}y \end{aligned} \tag{21}$$

The integration of Eq. (21) is carried out by the Gauss–Lobatto rule. In view of integrals along the beam axis, we take the case of $J_{i,yj}$ as an example:

$$\begin{aligned} J_{i,yj} &= \int_L N_{i,y}(y)N_j(y)\mathrm{d}y \\ &= \bigcup_{n=1}^{n_{\text{elem}}}\int_{L_n} N_{i,y}(y)N_j(y)\mathrm{d}y \\ &= \bigcup_{n=1}^{n_{\text{elem}}}\int_{-1}^{1} N_{i,\gamma}(\gamma)\tfrac{1}{|J_{1D}|}N_j(\gamma)|J_{1D}|\mathrm{d}\gamma \\ &= \bigcup_{n=1}^{n_{\text{elem}}}\sum_{m=1}^{n^m_{\text{glp}}} A_{im}N_j(\gamma_m)w_m \end{aligned} \tag{22}$$

where n_{elem} and n^m_{glp} are total number of beam elements and the Gauss–Lobatto points related to γ_m; $|J_{1D}|$ is the Jacobian determinant in the longitudinal direction; L_n is the length of the nth element; w_m is the weight pertaining to the Gauss–Lobatto point; the symbol $\bigcup_{n=1}^{n_{\text{elem}}}$ represents the operator that assembles the element stiffness matrix into the global stiffness matrix through the shared degrees of freedom; and the notation $\sum$ sums corresponding terms according to the subscript. Due to the property of $N_j(\gamma_m)=\delta_{jm}$, Eq. (22) can be further simplified as:

$$\bigcup_{n=1}^{n_{\text{elem}}}\sum_{m=1}^{n_{\text{glp}}} A_{im}N_j(\gamma_m)w_m = \bigcup_{n=1}^{n_{\text{elem}}}\sum_{m=1}^{n_{\text{glp}}} A_{ij}w_j \tag{23}$$

On the other hand, the computation of the cross-section integration depends on the chosen multilayered theory, i.e., ESL or LW.

In the case of ESL, $E^{\alpha\beta}_{\tau_{,\theta}s_{,\zeta}}$ may then be recast into the alternative expression:

$$\begin{aligned} E^{\alpha\beta}_{\tau_{,\theta}s_{,\zeta}} &= \int_\Omega \tilde{C}_{\alpha\beta}(x)F_{\tau,\theta}(x,z)F_{s,\zeta}(x,z)\mathrm{d}\Omega \\ &= \int_{-1}^{1}\int_{-1}^{1}\tilde{C}_{\alpha\beta}(\xi)F_{\tau,\theta}(\xi,\eta)F_{s,\zeta}(\xi,\eta)|J_{2D}|\mathrm{d}\xi\mathrm{d}\eta \\ &= \sum_{k=1}^{n_{\text{sub-domain}}}\int_{\xi^k_l}^{\xi^k_u}\int_{\eta^k_l}^{\eta^k_u}\tilde{C}_{\alpha\beta}(\xi^k)F_{\tau,\theta}(\xi^k,\eta^k)F_{s,\zeta}(\xi^k,\eta^k)|J_{2D}|\mathrm{d}\xi^k\mathrm{d}\eta^k \\ &= \sum_{k=1}^{n_{\text{sub-domain}}}\sum_{i=1}^{n^i_{\text{glp}}}\sum_{j=1}^{n^j_{\text{glp}}}\tilde{C}_{\alpha\beta}(\xi^k_i)F_{\tau,\theta}(\xi^k_i,\eta^k_j)F_{s,\zeta}(\xi^k_i,\eta^k_j)|J_{2D}|w^k_i w^k_j \end{aligned} \tag{24}$$

On the contrary, LW deals with $E^{\alpha\beta}_{\tau_{,\theta}s_{,\zeta}}$ in another possible way:

$$\begin{aligned} E^{\alpha\beta}_{\tau_{,\theta}s_{,\zeta}} &= \int_\Omega \tilde{C}_{\alpha\beta}(x)F_{\tau,\theta}(x,z)F_{s,\zeta}(x,z)\mathrm{d}\Omega \\ &= \bigcup_{k=1}^{n_{\text{sub-domain}}}\int_{-1}^{1}\int_{-1}^{1}\tilde{C}_{\alpha\beta}(\xi^k)F_{\tau,\theta}(\xi^k,\eta^k)F_{s,\zeta}(\xi^k,\eta^k)\left|J^k_{2D}\right|\mathrm{d}\xi^k\mathrm{d}\eta^k \\ &= \bigcup_{k=1}^{n_{\text{sub-domain}}}\sum_{i=1}^{n^i_{\text{glp}}}\sum_{j=1}^{n^j_{\text{glp}}}\tilde{C}_{\alpha\beta}(\xi^k_i)F_{\tau,\theta}(\xi^k_i,\eta^k_j)F_{s,\zeta}(\xi^k_i,\eta^k_j)\left|J^k_{2D}\right|w^k_i w^k_j \end{aligned} \tag{25}$$

$\sum_{k=1}^{n_{\text{sub-domain}}}$ represents the direct summation of kinematic terms in ESL, whereas $\bigcup_{k=1}^{n_{\text{sub-domain}}}$ denotes the assembly of cross-section expansion terms in LW. Additionally, the interval of the Gauss–Lobatto integration in ESL is scaled with respect to the geometrical size of the sub-domain, from [-1, +1] to $[\xi^{k_l},\xi^{k_u}]$ or $[\eta^{k_l},\eta^{k_u}]$. This operation marginally complicates the pre-processing process in ESL compared to that in LW. However, the increasing computation cost associated with the preceding transformation in ESL can be neglected in comparison with the layer-dependent feature in LW. Besides, more Gauss–Lobatto points should be allotted to correctly compute the 2D integral since the material coefficients in $\tilde{C}$ are functions of the isoparametric coordinate ξ. To be specific, for F_τ with the jth order, $j+4$ Gauss–Lobatto points are employed in the computation of Eq. (24) or (25). However, $j+2$ Gauss–Lobatto points are needed for computing the cross-section integral in CSCL structures. As a result, computational costs are expected to increase marginally in the analysis of VSCLs.

As far as the harmonic motion is concerned, the solution can be assumed to the following manner

$$\mathbf{u}_{sj} = \mathbf{U}_{sj}e^{i\omega t} \tag{26}$$

where $\mathbf{U}_{sj}$ is the amplitude of displacement unknowns; ω is the angular frequency; and i^2 is equal to -1. By substituting Eq. (26), Eq. (20), and

Eq. (19) into Eq. (17), a linear system of the algebraic equations of motion is given by:

$$\left(\mathbf{K}^{\tau sij}-\omega^2\mathbf{M}^{\tau sij}\right)\mathbf{U}_{sj}=0 \tag{27}$$

The implementation of the matrix assembly can be ensured by expanding the fundamental nucleus over the indexes τ, s, i, and j. Generally speaking, the matrix assembly over the cross-section domain can be done in the preliminary stage. Following that, the matrix assembly of DQFEM-defined beam elements can be completed. Note that the assembly rule of the stiffness and mass matrices of VSCLs is identical to that of CSCLs. For this reason, readers can refer to the literature [30] for a more detailed implementation of global matrices. Once global matrices are obtained, the eigenvalue problem can be finally solved via the imposition of boundary conditions.

5. Numerical results

The solutions to the free vibration problem of VSCL beams and plates have been presented in this section obtained by the DQFEM-based CUF-IHLE model. Numerical calculations are performed in ESL and LW descriptions generated by IHLE kinematics to show the advantage of each model. The validation procedure is divided into two parts: the first part focuses on the VSCL beams with a group of fibre paths subjected to clamped–clamped (C–C) and clamped-free (C-F) boundary conditions; the second part addresses VSCL plates, paying special attention to the effect of lamination schemes and thickness-to-width ratios on frequencies. Unless stated otherwise, the polynomial order of internal modes in ESL models is p, whereas it is $p-1$ in LW models when the polynomial order of side modes is given as p.

5.1. VSCL beam

The preliminary validation addresses the free vibration problem of the symmetric three-layer VSCL beam with lamination schemes $[+\langle T_0/T_1\rangle, -\langle T_0/T_1\rangle, +\langle T_0/T_1\rangle]$. The geometrical size of the beam is given as follows: the width $b=0.2$ m, the height $h=0.2$ m, and the length $L=1$ m. Orthotropic material properties correspond to the following values: Young moduli $E_{11}=288$ GPa and $E_{22}=E_{33}=7.2$ GPa; Shear moduli $G_{12}=G_{13}=4.32$ GPa and $G_{23}=3.6$ GPa; Poisson ratio $\nu_{12}=\nu_{13}=\nu_{23}=0.25$; Material density $\rho=1540$ kg/m^3. Two types of boundary conditions are considered: the clamped and free.

Subsequently, the convergence study of the first non-dimensional angular frequency $\omega^*=\omega L^2/h\sqrt{\rho/E_{22}}$ in terms of C–C and C-F boundary conditions is demonstrated in Table 1 and 2. The results obtained with DQFEM are compared with the FEM solutions in the literature [47] when T_0 and T_1 range over the interval [0°, 45°]. The beam element is defined as ϑBβ, where ϑ and β represent the number of elements and the nodes in a single element. The number of degrees of freedoms (DOFs) for each method is also reported in the last column of two tables. As illustrated in the tables, DQFEM converges rather rapidly, computing smaller values with far fewer DOFs than FEM. Besides, the clamped boundary condition increases the value of the first angular frequency featured by the bending mode. In this regard, angle-ply lamination schemes $(T_0\neq 0^\circ, T_1\neq 0^\circ)$ soften the bending stiffness, leading to the reduction of the first angular frequency. On the other hand, the discrepancy between DQFEM and FEM results is more pronounced when T_0 is equal to 45° and T_1 falls inside a certain range [20°, 60°]. According to convergence analyses, the 1B9 element is selected to evaluate the influence of different expansion orders in the following discussion.

As for cross-section discretization schemes, 1 sub-domain is developed for the ESL model and 6 sub-domains for the LW model. It should be noted that the LW model normally employs a single domain per layer for CSCL beams. This operation presents a risk of numerical instability in VSCL beams since the function used to describe the fibre path includes an absolute value. This mathematical issue can be solved by adding a mathematical boundary at the discontinuous point, namely, two domains per layer. The notation ψIHL$\xi\times\zeta$ refers to the number of sub-domains (ψ) and the polynomial order ($\xi\times\zeta$) in the x and z directions.

Tables 3 and 4 include the first four modal values in two different kinds of boundary conditions with various expansion orders. To make a direct comparison of ESL and LW approaches, Three kinds of fibre orientation angles are considered: $[+\langle 45^\circ/45^\circ\rangle, -\langle 45^\circ/45^\circ\rangle, +\langle 45^\circ/45^\circ\rangle]$, $[+\langle 0^\circ/60^\circ\rangle, -\langle 0^\circ/60^\circ\rangle, +\langle 0^\circ/60^\circ\rangle]$, $[+\langle 45^\circ/40^\circ\rangle, -\langle 45^\circ/40^\circ\rangle, +\langle 45^\circ/40^\circ\rangle]$. Some comments arise from the preceding two tables:

(1) In general, the first-order expansion (IHL1 × 1) in the ESL model is only appropriate for the quick computation of the first bending mode on plane yz. For the special case of $T_0=0^\circ, T_1=60^\circ$, the mode exchange between the mode 1 and 2 even occurs in IHL1 × 1. In other words, IHL1 × 1 fails in the analysis of VSCL beams.
(2) In the vast majority of cases, the first four modal values given by the ESL model achieve satisfactory convergence for the third-order model (IHL3 × 3) except for the case of

Table 1
Convergence of the first non-dimensional angular frequency for the VSCL beam obtained with the ESL models of the first-order expansion (C–C).

Method	T_0: 0°				45°				DOFs
	T_1: 0°	20°	40°	60°	0°	20°	40°	60°	
FEM-40B2 [47]	11.678	11.324	10.935	10.610	10.854	9.766	8.531	7.631	369
DQFEM-1B5	11.666	11.300	10.912	10.585	10.832	9.703	8.320	7.464	60
DQFEM-1B7	11.672	11.304	10.916	10.588	10.835	9.681	8.180	7.314	84
DQFEM-1B9	11.672	11.304	10.916	10.588	10.835	9.680	8.176	7.310	108

Table 2
Convergence of the first non-dimensional angular frequency for the VSCL beam obtained with the ESL models of the first-order expansion (C-F).

Method	T_0: 0°				45°				DOFs
	T_1: 0°	20°	40°	60°	0°	20°	40°	60°	
FEM-40B2 [47]	4.456	3.791	3.384	3.136	3.320	2.458	1.867	1.551	369
DQFEM-1B5	4.454	3.748	3.353	3.110	3.292	2.367	1.650	1.408	60
DQFEM-1B7	4.454	3.748	3.352	3.108	3.291	2.363	1.640	1.398	84
DQFEM-1B9	4.454	3.748	3.352	3.108	3.291	2.363	1.639	1.397	108

Table 3
First four non-dimensional angular frequencies of CSCL and VSCL beams for the C–C boundary condition.

Expansion order	mode 1[a]	mode 2[b]	mode 3[c]	mode 4[d]	DOFs
		ESL model ($T_0 = 45°, T_1 = 45°$)			
1IHL1 × 1	7.862	**18.835**	**19.734**	**16.974**	108
1IHL2 × 2	7.568	10.537	**17.072**	**16.373**	243
1IHL3 × 3	7.062	9.883	**15.403**	**15.378**	432
1IHL4 × 4	7.043	9.570	15.262	15.341	675
		LW model ($T_0 = 45°, T_1 = 45°$)			
6IHL1 × 1	7.212	13.757	**17.149**	**15.693**	324
6IHL2 × 2	6.983	9.583	15.246	15.314	783
6IHL3 × 3	6.926	9.322	15.056	15.193	1404
		ESL model ($T_0 = 0°, T_1 = 60°$)			
1IHL1 × 1	10.588	**19.252**	**18.370**	21.692	108
1IHL2 × 2	10.514	14.163	16.860	21.506	243
1IHL3 × 3	9.760	13.050	14.838	20.341	432
1IHL4 × 4	9.708	11.494	14.734	20.222	675
		LW model ($T_0 = 0°, T_1 = 60°$)			
6IHL1 × 1	10.095	13.170	16.055	20.967	324
6IHL2 × 2	9.722	11.234	14.376	20.251	783
6IHL3 × 3	9.615	10.247	13.757	19.898	1404
		ESL model ($T_0 = 45°, T_1 = 40°$)			
1IHL1 × 1	8.176	**20.584**	**20.371**	**17.385**	108
1IHL2 × 2	7.873	11.953	**17.390**	**16.759**	243
1IHL3 × 3	7.315	11.068	15.709	15.775	432
1IHL4 × 4	7.291	10.594	15.570	15.715	675
		LW model ($T_0 = 45°, T_1 = 40°$)			
6IHL1 × 1	7.483	15.722	**17.701**	**16.041**	324
6IHL2 × 2	7.227	10.664	15.562	15.677	783
6IHL3 × 3	7.158	10.233	15.341	15.538	1404

[a] First flexural mode on plane *yz*
[b] First flexural mode on plane *xy*
[c] First torsional mode
[d] Second flexural mode on plane *yz*

Table 4
First four non-dimensional angular frequencies of CSCL and VSCL beams for the C-F boundary condition.

Expansion order	mode 1[a]	mode 2[b]	mode 3[c]	mode 4[d]	DOFs
		ESL model ($T_0 = 45°, T_1 = 45°$)			
1IHL1 × 1	1.530	3.308	**8.590**	**7.818**	108
1IHL2 × 2	1.440	1.554	**7.969**	**7.460**	243
1IHL3 × 3	1.379	1.503	**7.274**	**7.017**	432
1IHL4 × 4	1.374	1.467	**7.236**	**6.984**	675
		LW model ($T_0 = 45°, T_1 = 45°$)			
6IHL1 × 1	1.388	2.179	**7.800**	**7.104**	324
6IHL2 × 2	1.348	1.456	**7.242**	**6.899**	783
6IHL3 × 3	1.334	1.423	**7.173**	**6.827**	1404
		ESL model ($T_0 = 0°, T_1 = 60°$)			
1IHL1 × 1	3.108	3.463	8.380	12.387	108
1IHL2 × 2	**3.089**	**2.360**	7.991	12.321	243
1IHL3 × 3	**2.773**	**2.319**	7.225	11.369	432
1IHL4 × 4	**2.760**	**1.900**	7.190	11.316	675
		LW model ($T_0 = 0°, T_1 = 60°$)			
6IHL1 × 1	**2.970**	**2.133**	7.674	11.919	324
6IHL2 × 2	**2.724**	**1.895**	7.091	11.278	783
6IHL3 × 3	**2.679**	**1.783**	6.812	11.133	1404
		ESL model ($T_0 = 45°, T_1 = 40°$)			
1IHL1 × 1	1.639	3.684	**8.802**	**8.185**	108
1IHL2 × 2	1.542	1.756	**8.075**	**7.826**	243
1IHL3 × 3	1.459	1.685	**7.464**	**7.231**	432
1IHL4 × 4	1.452	1.622	**7.437**	**7.177**	675
		LW model ($T_0 = 45°, T_1 = 40°$)			
6IHL1 × 1	1.479	2.540	**8.023**	**7.382**	324
6IHL2 × 2	1.420	1.616	**7.402**	**7.116**	783
6IHL3 × 3	1.401	1.556	**7.338**	**7.020**	1404

[a] First flexural mode on plane *yz*
[b] First flexural mode on plane *xy*
[c] First torsional mode
[d] Second flexural mode on plane *yz*

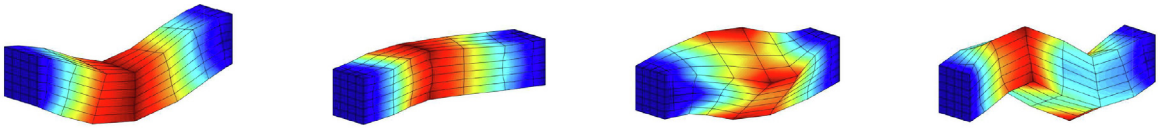

(a) First flexural mode on plane yz ($T_0 = 45°, T_1 = 45°$) (b) First flexural mode on plane xy ($T_0 = 45°, T_1 = 45°$) (c) First torsional mode ($T_0 = 45°, T_1 = 45°$) (d) Second flexural mode on plane yz ($T_0 = 45°, T_1 = 45°$)

Fig. 5. First four mode shapes in the 3D space for the C–C condition.

$T_0 = 45°, T_1 = 45°$ in the C–C boundary condition, where IHL4 × 4 is needed to identify the correct order of appearance of the mode 3 and 4.

(3) In terms of the LW model, the first four modes can be accurately captured by the low-order model (IHL2 × 2) in view of values and order of appearance, while its DOFs are almost twice higher than those of IHL3 × 3 generated by the ESL model.

(4) In the case of the C-F boundary condition, the sequence of modal appearance is quite sensitive to the values of T_0 and T_1. Specifically, the first flexural mode on plane xy tends to appear before the first flexural mode on plane xy when T_0 is close to 0° and T_1 to 90°. On the other hand, the second flexural mode on plane yz is apt to manifest earlier than the first torsional mode when T_0 and T_1 are both in close proximity to 45°.

Figs. 5 and 6 give the 3D plots of the first four modes under different boundary conditions. From the figures, we can clearly see the first mode tends to be the first bending mode on plane xy instead of on plane yz. Furthermore, the second bending mode on plane yz is more or less mixed in with the component of the torsional mode in the angle-ply lamination scheme. This phenomenon is more prominent in the C-F boundary condition, where it is difficult to distinguish the first torsional mode and second bending mode on plane yz when both T_0 and T_1 are close to 45°.

5.2. VSCL plate

A three-layer VSCL plate is considered to further verify the correctness of the proposed model. Different from the cross-section of a beam, whose dimension in the width direction is of high proximity to that in the thick direction, the width and length of a plate are predominant with respect to the thickness. Accordingly, expansion orders in the two orthogonal dimensions should be distinct in the IHLE model, thus saving computational efforts.

The first investigation of this section is related to the VSCL plates with different thickness-to-width ratios (0.01 and 0.1). This kind of analysis has been performed by Viglietti et al. [36], who used the h-version finite element method based on 1D CUF-LE models. The length and width of the plate are equal to 1 m and the orthotropic material is employed for each layer and has the following properties: $E_{11} = 173.0$ GPa, $E_{22} = E_{33} = 7.2$ GPa, $\nu_{12} = \nu_{13} = \nu_{23} = 0.29$, $G_{12} = G_{13} = G_{23} = 3.76$ GPa, $\rho = 1540$ kg/m^3. The stacking sequence

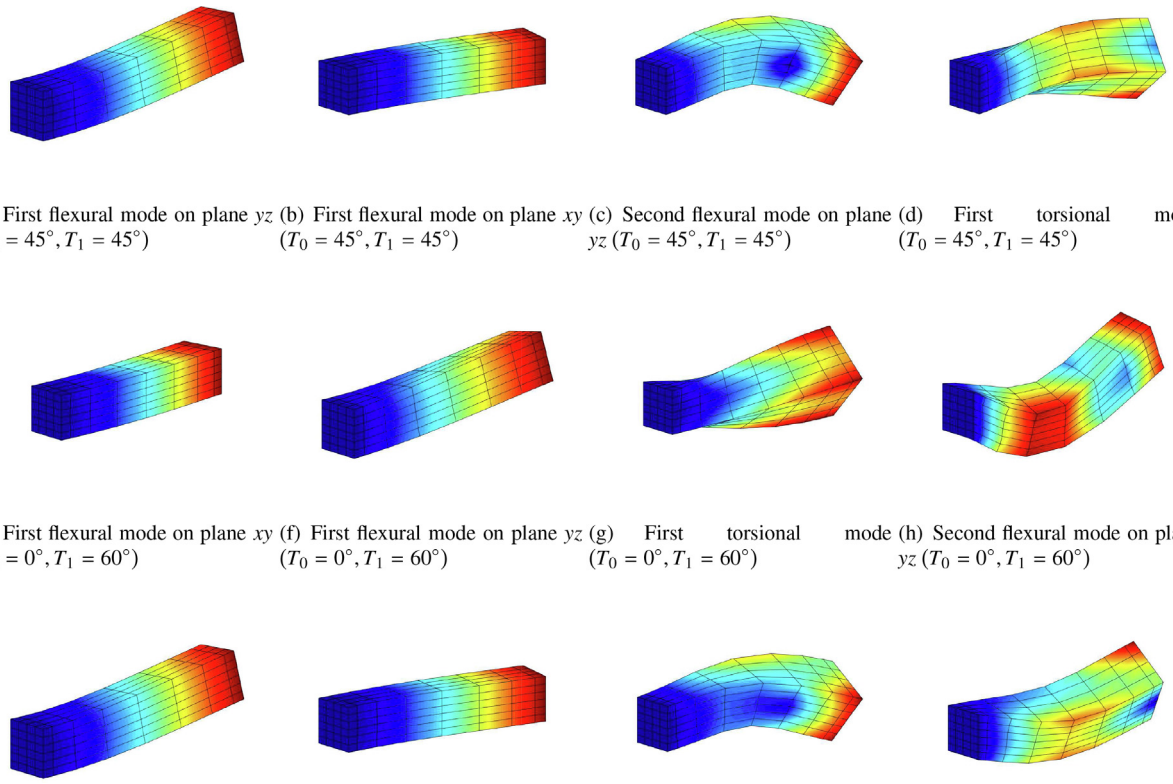

(a) First flexural mode on plane yz ($T_0 = 45°, T_1 = 45°$) (b) First flexural mode on plane xy ($T_0 = 45°, T_1 = 45°$) (c) Second flexural mode on plane yz ($T_0 = 45°, T_1 = 45°$) (d) First torsional mode ($T_0 = 45°, T_1 = 45°$)

(e) First flexural mode on plane xy ($T_0 = 0°, T_1 = 60°$) (f) First flexural mode on plane yz ($T_0 = 0°, T_1 = 60°$) (g) First torsional mode ($T_0 = 0°, T_1 = 60°$) (h) Second flexural mode on plane yz ($T_0 = 0°, T_1 = 60°$)

Fig. 6. First four mode shapes in the 3D space for the C-F condition.

Table 5
First seven natural frequencies (Hz) for the VSCL plate with different heights.

Height	Model	mode 1	mode 2	mode 3	mode 4	mode 5	mode 6	mode 7	DOFs
0.1	*p*-FEM-TSDT [36]	614.11	909.55	1233.02	1338.63	1485.64	1798.60	1932.28	-[a]
	h-FEM-LE [36]	609.79	903.63	1216.00	1328.41	1469.33	1774.84	1930.15	9261
	h-FEM-3D [36]	607.24	897.04	1208.40	1314.14	1458.18	1753.52	1916.57	95000
				ESL model					
	1B7 + 1IHL6 × 2	636.83	949.13	1283.71	1405.31	1558.49	1917.77	2064.10	441
	1B9 + 1IHL8 × 2	634.88	943.47	1275.36	1414.05	1551.60	1906.44	2036.82	729
	1B11 + 1IHL10 × 2	633.77	941.62	1271.85	1394.22	1539.66	1885.31	2017.45	1089
	1B11 + 1IHL10 × 3	610.19	905.38	1214.71	1331.24	1469.82	1781.82	1926.40	1452
	1B11 + 1IHL10 × 4	610.05	905.13	1214.30	1330.58	1469.13	1780.44	1924.89	1815
				LW model					
	1B8 + 6IHL4 × 2	621.23	911.63	1248.40	1346.84	1503.39	1810.49	1938.15	1080
	1B11 + 6IHL5 × 2	619.02	908.86	1239.98	1330.19	1490.34	1789.06	1928.57	1749
	1B11 + 6IHL5 × 3	608.89	899.54	1214.51	1318.33	1465.24	1764.96	1910.28	2640
	1B11 + 6IHL5 × 4	608.07	898.25	1211.82	1315.50	1461.58	1756.51	1908.49	3531
0.01	*p*-FEM-TSDT [36]	92.26	130.82	195.19	237.86	274.99	282.67	340.09	–[a]
	h-FEM-LE [36]	94.44	135.36	206.4	247.05	287.67	307.89	361.64	9261
	h-FEM-3D [36]	92.65	131.50	196.86	239.23	276.76	286.34	342.84	95000
				ESL model					
	1B7 + 1IHL6 × 2	94.43	135.56	202.78	244.40	289.99	358.82	474.94	441
	1B9 + 1IHL8 × 2	92.53	131.36	196.30	239.25	277.84	299.44	353.22	729
	1B11 + 1IHL10 × 2	92.42	131.11	195.73	238.55	275.96	284.25	341.74	1089
	1B11 + 1IHL10 × 3	92.30	130.95	195.47	237.92	275.24	283.78	340.86	1452
	1B11 + 1IHL10 × 4	92.30	130.94	195.46	237.92	275.24	283.77	340.86	1815
				LW model					
	1B8 + 6IHL4 × 2	94.34	134.57	204.92	247.71	296.43	300.82	371.92	1080
	1B11 + 6IHL5 × 2	92.62	131.37	195.99	239.79	279.29	284.91	346.27	1749
	1B11 + 6IHL5 × 3	92.56	131.29	195.87	239.41	278.79	284.66	345.62	2640
	1B11 + 6IHL6 × 4	92.33	130.96	195.41	238.08	275.56	283.64	341.27	4191

[a] Not provided by the theory

Table 6
Geometrical sizes and material properties for the VSCL plate

a (m)	b (m)	h (m)	E_{11}(GPa)	E_{22}(GPa)	E_{33}(GPa)	ν_{12}	ν_{13}	ν_{23}	G_{12}(GPa)	G_{13}(GPa)	G_{23}(GPa)	ρ(kg/m^3)
1	1	0.2	138	8.96	8.96	0.3	0.3	0.3	7.1	7.1	7.1	1

is assumed to be $[\langle 0^\circ/45^\circ\rangle, \langle -45^\circ/-60^\circ\rangle, \langle 0^\circ/45^\circ\rangle]$ and the boundary condition is four edges clamped.

Table 5 shows the first seven natural frequencies of the clamped plates featured by diverse thickness-to-length ratios. The results obtained by the CUF-IHLE models in terms of ESL and LW approaches are compared with those available in the literature [36]. In detail, *p*-FEM-TSDT corresponds to the numerical implementation by the *p*-FEM based on the third-order shear deformation theory, and the *h*-FEM-3D represents the 3D FEM model created by the Nastran software. Some useful conclusions can be drawn from the table:

(1) The present method can yield almost identical values as those in the reference while keeping the computational cost much lower than *h*-FEM-LE and *h*-FEM-3D models.
(2) For the thick plate, ESL models accounting for the quadratic-polynomial expansion in the thickness direction are unable to yield accurate modal values, especially in the high-frequency range. The expansion order in the thickness direction should be higher than 3 to get convergent results both for ESL and LW models.
(3) Due to the minor role played by shear deformations in thin plates, increasing the expansion order in the thickness direction has little effect on the accuracy of the assessment. On the contrary, a significant improvement in accuracy can be observed as the polynomial degrees both in the length and width direction increase. The mechanism behind this phenomenon appears to be associated with the inhibition of the locking, which is more pronounced when the stress calculations of thin shell structures are performed using standard lower-order FEM models. By increasing the number of elements and the order of interpolation functions, two viable solutions to the locking problem become apparent (see the results of *h*-FEM-3D and 1B11 + 1IHL10 × 2).

The next assessment is devoted to the analysis of the VSCL plates with symmetric and unsymmetric lamination schemes. For comparison purpose, the same geometrical sizes and material properties as those in the literature [26] are considered, as listed in Table 6. The fibre orientation angle for the symmetric condition can be expressed as $[\langle 15^\circ/-15^\circ\rangle, \langle 15^\circ/-30^\circ\rangle, \langle 15^\circ/-15^\circ\rangle]$ and that for the unsymmetric case as $[\langle 15^\circ/-15^\circ\rangle, \langle 15^\circ/-30^\circ\rangle, \langle 15^\circ/-45^\circ\rangle]$. The first six modal values are shown in Table 7, which are produced using proposed ESL and LW approaches as well as the LW method in Yazdani and Ribeiro [26], where in-plane displacements vary linearly through the thickness, and out-of-plane counterparts are constant in the thickness direction. A combination of different numbers of nodes and various cross-section expansion orders is also included. Fig. 7 gives the 3D plot of the mode shapes corresponding to the values in Table 5 and 7. Out of these results, the following remarks can be made:

(1) Small variations in the fibre orientation angles result in the alteration of modal values to different degrees. In other words, increasing the fibre orientation angle at the edge does not lead to an increase in all modal values.

Table 7
First six natural frequencies (Hz) for the VSCL plate with different lamination schemes.

Fibre Path	Model	mode 1	mode 2	mode 3	mode 4	mode 5	mode 6	DOFs
$[\langle 15°/-15°\rangle,$	LW [26]	40239.08	57104.54	65239.73	76380.43	83762.36	88507.89	–[a]
$\langle 15°/-30°\rangle,$			ESL model					
$\langle 15°/-15°\rangle]$	1B7 + 1IHL6 × 2	41350.50	58827.96	65617.44	78192.70	86161.00	90872.87	441
	1B9 + 1IHL8 × 2	41291.67	58441.70	65543.68	78000.07	85316.35	90392.25	729
	1B11 + 1IHL10 × 2	41277.27	58418.45	65522.87	77969.88	85308.01	90336.93	1089
	1B11 + 1IHL10 × 3	39684.58	56720.05	65503.62	74863.28	83067.08	87248.73	1452
	1B11 + 1IHL10 × 4	39654.67	56658.38	65401.86	74787.22	82932.15	87133.57	1815
				LW model				
	1B8 + 6IHL4 × 2	40496.52	57313.24	65452.77	76471.70	84380.25	88906.64	1080
	1B11 + 6IHL5 × 2	40466.31	57238.08	65418.05	76431.10	83389.68	88802.49	1749
	1B11 + 6IHL5 × 3	39659.69	56655.64	65370.38	74792.21	82920.31	87146.68	2640
	1B11 + 6IHL5 × 4	39593.98	56607.05	65369.06	74568.31	82879.02	86942.42	3531
$[\langle 15°/-15°\rangle,$	LW [26]	39252.31	57247.66	65834.81	75702.50	84590.95	88507.89	–a
$\langle 15°/-30°\rangle,$			ESL model					
$\langle 15°/-45°\rangle]$	1B7 + 1IHL6 × 2	40502.92	59061.05	66333.76	77739.18	86986.54	91185.84	441
	1B9 + 1IHL8 × 2	40328.27	58624.88	66190.05	77413.26	86203.57	90443.03	729
	1B11 + 1IHL10 × 2	40286.93	58583.16	66155.54	77346.46	86183.95	90334.34	1089
	1B11 + 1IHL10 × 3	38789.63	56909.35	65848.34	74368.23	83921.22	87249.58	1452
	1B11 + 1IHL10 × 4	38733.53	56822.12	65823.07	74266.55	83757.41	87082.20	1815
				LW model				
	1B8 + 6IHL4 × 2	39505.98	57440.30	66014.20	75946.54	85175.20	89057.60	1080
	1B11 + 6IHL5 × 2	39453.46	57349.27	65952.79	75766.21	84181.34	88827.62	1749
	1B11 + 6IHL5 × 3	38749.45	56820.19	65801.11	74325.65	83736.68	87127.07	2640
	1B11 + 6IHL5 × 4	38689.07	56775.33	65782.10	74130.82	83700.43	86930.47	3531

[a] Not provided by the theory

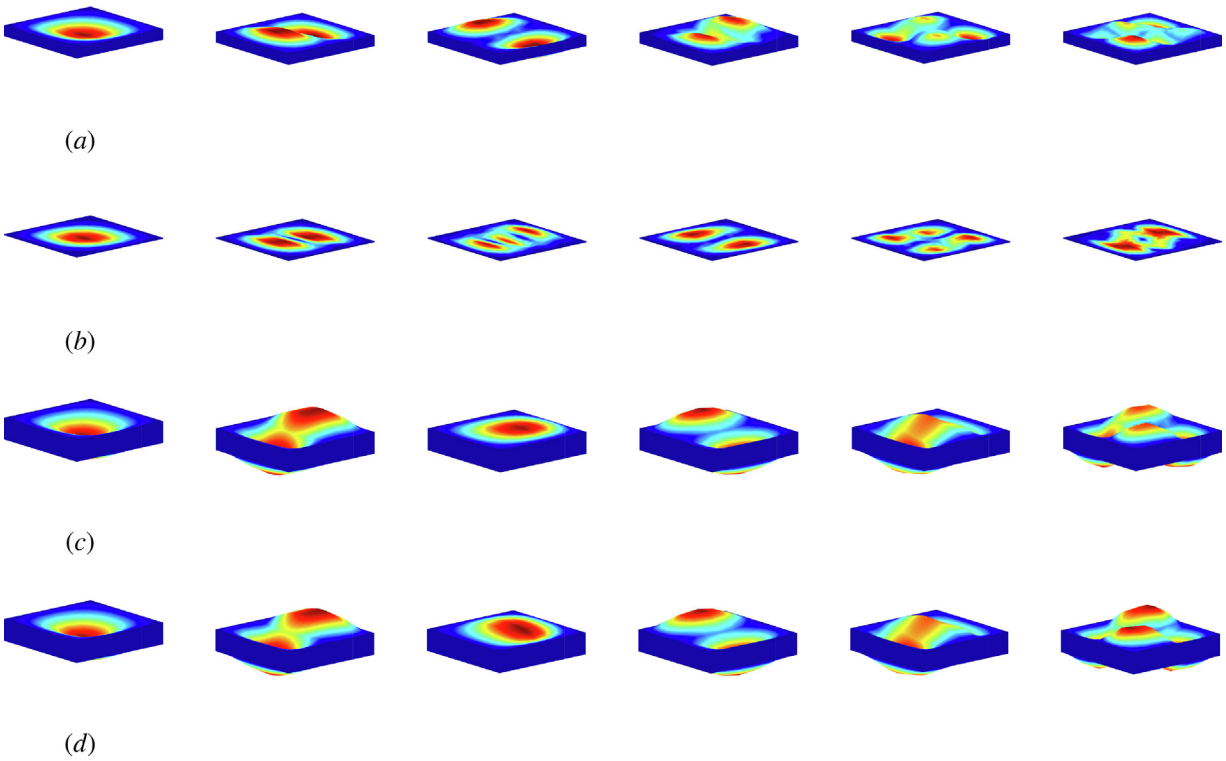

Fig. 7. Mode shapes of: (*a*) a VSCL plate ($h = 0.01$) with $[\langle 0°/45°\rangle, \langle -45°/-60°\rangle, \langle 0°/45°\rangle]$; (*b*) a VSCL plate ($h = 0.1$) with $[\langle 0°/45°\rangle, \langle -45°/-60°\rangle, \langle 0°/45°\rangle]$; (*c*) a symmetric VSCL plate with $[\langle 15°/-15°\rangle, \langle 15°/-30°\rangle, \langle 15°/-15°\rangle]$ (*d*) an unsymmetric VSCL plate with $[\langle 15°/-15°\rangle, \langle 15°/-30°\rangle, \langle 15°/-45°\rangle]$.

(2) The modal values provided by Yazdani and Ribeiro [26] fall between those computed by 1B8 + 6IHL4 × 2 and 1B11 + 6IHL5 × 4, which means the LW model in Yazdani and Ribeiro [26] is actually a special case of our developed LW model.

(3) Mode switching between the third and fourth modes occurs as the thickness-to-width ratio decreases. On the other hand, when the thickness-to-width ratio is greater than 0.2, mode 3 is dominated by the shear deformation on plane *xy*. Another interest-

ing fact can be observed in symmetric and unsymmetric VSCL plates, in which a slight alteration of fibre orientation angles has little effect on the profiles of 3D mode shapes.

6. Conclusions

A novel unified quasi-3D solution is developed for free vibration analyses of tow-steered composite laminates in this work. The study is carried out using a mix of the Carrera Unified Formulation (CUF) model based on improved hierarchical Legendre expansion (IHLE) and the differential quadrature finite element method (DQFEM). Numerous examples have been performed to illustrate the high numerical accuracy and efficiency of the present model, including beams and plates with a variety of geometric sizes and lamination schemes. Several significant conclusions can be drawn from numerical results:

1. The DQFEM-based beam element requires significantly fewer degrees of freedom than the FEM-based one. Moreover, the further away fibre orientation is from 0°, the better the trade-off between precision and computational cost that DQFEM can deliver.
2. A possible mode switching phenomenon may arise in VSCL beams when a lower-order expansion is adopted in the CUF-IHLE model. Thus, it is not recommended to use Euler–Bernoulli or Timoshenko beam theory in this type of analysis.
3. In view of VSCL plates, the higher-order Equivalent Single Layer (ESL) model may attain nearly the same degree of accuracy as the higher-order Layer-Wise (LW) model at a lower computational cost. Additionally, as thickness-to-width ratios grow, non-classical modes, such as shear mode, may appear early.
4. For the computation of thick VSCL plates, it is necessary to refine the cross-section kinematics in the thickness direction, whereas such refinement in the width direction results in significantly faster convergence for the case of thin VSCL plates.

The idea of placing fibres along curved routes offers the designer great flexibility to improve the mechanical performance of laminated structures. The developed CUF-IHLE-based DQFEM approach can be further applied to the optimization study of the dynamic characteristics of VSCL structures with guaranteed accuracy and efficiency.

CRediT authorship contribution statement

Yang Yan: Conceptualization, Formal analysis, Investigation, Methodology, Validation, Visualization, Writing - original draft, Writing - review & editing. **Bo Liu:** Validation, Funding acquisition. **Yufeng Xing:** Writing - review & editing, Supervision, Funding acquisition. **Erasmo Carrera:** Methodology, Validation, Investigation, Writing - review & editing. **Alfonso Pagani:** Conceptualization, Resources, Writing - review & editing, Supervision, Funding acquisition.

Declaration of Competing Interest

The authors declare that they have no known competing financial interests or personal relationships that could have appeared to influence the work reported in this paper.

Acknowledgments

Yang Yan, Bo Liu and Yufeng Xing acknowledge funding from the National Natural Science Foundation of China (Grant No. 12002012, 11772031, 11972004, 11402015, 11872090, 11672019). Alfonso Pagani acknowledges funding from the European Research Council (ERC) under the European Union's Horizon 2020 research and innovation programme (Grant agreement No. 850437).

References

[1] Lozano GG, Tiwari A, Turner C, Astwood S. A review on design for manufacture of variable stiffness composite laminates. Proc Inst Mech Eng Part B 2016;230(6):981–92.
[2] Leissa AW, Martin AF. Vibration and buckling of rectangular composite plates with variable fiber spacing. Compos Struct 1990;14(4):339–57.
[3] Kuo SY, Shiau LC. Buckling and vibration of composite laminated plates with variable fiber spacing. Compos Struct 2009;90(2):196–200.
[4] Her SC. Stress analysis of ply drop-off in composite structures. Compos Struct 2002;57(1–4):235–44.
[5] Paluch B, Grediac M, Faye A. Combining a finite element programme and a genetic algorithm to optimize composite structures with variable thickness. Compos Struct 2008;83(3):284–94.
[6] Sliseris J, Rocens K. Optimal design of composite plates with discrete variable stiffness. Compos Struct 2013;98:15–23.
[7] Vescovini R, Oliveri V, Pizzi D, Dozio L, Weaver PM. A semi-analytical approach for the analysis of variable-stiffness panels with curvilinear stiffeners. Int J Solids Struct 2020;188:244–60.
[8] Gürdal Z, Tatting BF, Wu CK. Variable stiffness composite panels: effects of stiffness variation on the in-plane and buckling response. Compos Part A 2008;39(5):911–22.
[9] Raju G, Wu Z, Weaver PM. Buckling and postbuckling of variable angle tow composite plates under in-plane shear loading. Int J Solids Struct 2015;58:270–87.
[10] Hyer MW, Lee HH. The use of curvilinear fiber format to improve buckling resistance of composite plates with central circular holes. Compos Struct 1991;18(3):239–61.
[11] Gürdal Z, Olmedo R. In-plane response of laminates with spatially varying fiber orientations-variable stiffness concept. AIAA J 1993;31(4):751–8.
[12] Tatting BF, Gürdal Z. Design and manufacture of elastically tailored tow placed plates. Technical Report NASA/CR-2002-211919, National Aeronautics and Space Administration, Langley Research Center, Hampton, Virginia; 2002..
[13] Jegley D, Tatting BF, Gürdal Z. Optimization of elastically tailored tow-placed plates with holes. In: Proceedings of the 44th AIAA/ASME/ASCE/AHS/ASC Structures, Structural Dynamics and Materials Conference, Norfolk, Virginia, 2003; p. 1420..
[14] Wu C, Gürdal Z, Starnes J. Structural response of compression-loaded, tow-placed, variable stiffness panels. In: Proceedings of the 44th AIAA/ASME/ASCE/AHS/ASC Structures, Structural Dynamics and Materials Conference, Denver, Colorado, 2002; p. 1512..
[15] Wu Z, Weaver PM, Raju G, Kim BC. Buckling analysis and optimisation of variable angle tow composite plates. Thin-Walled Struct 2012;60:163–72.
[16] Alhajahmad A, Abdalla MM, Gürdal Z. Design tailoring for pressure pillowing using tow-placed steered fibers. J Aircr 2008;45(2):630–40.
[17] Akhavan H, Ribeiro P. Natural modes of vibration of variable stiffness composite laminates with curvilinear fibers. Compos Struct 2011;93(11):3040–7.
[18] Honda S, Narita Y. Natural frequencies and vibration modes of laminated composite plates reinforced with arbitrary curvilinear fiber shape paths. J Sound Vib 2012;331(1):180–91.
[19] Akbarzadeh AH, Nik MA, Pasini D. Vibration responses and suppression of variable stiffness laminates with optimally steered fibers and magnetostrictive layers. Compos Part B 2016;91:315–26.
[20] Venkatachari A, Natarajan S, Haboussi M, Ganapathi M. Environmental effects on the free vibration of curvilinear fibre composite laminates with cutouts. Compos Part B 2016;88:131–8.
[21] Tan P, Nie GJ. Free and forced vibration of variable stiffness composite annular thin plates with elastically restrained edges. Compos Struct 2016;149:398–407.
[22] Farsadi T, Asadi D, Kurtaran H. Fundamental frequency optimization of variable stiffness composite skew plates. Acta Mech 2021;232(2):555–73.
[23] Guenanou A, Houmat A, Hachemi M, Chebout R, Bachari K. Free vibration of shear deformable symmetric vscl elliptical plates by a curved rectangular *p*-element. Mech Adv Mater Struct, In press..
[24] Zhao W, Kapania RK. Prestressed vibration of stiffened variable-angle tow laminated plates. AIAA J 2019;57(6):2575–93.
[25] Houmat A. Three-dimensional free vibration analysis of variable stiffness laminated composite rectangular plates. Compos Struct 2018;194:398–412.
[26] Yazdani S, Ribeiro P. A layerwise p-version finite element formulation for free vibration analysis of thick composite laminates with curvilinear fibres. Compos Struct 2015;120:531–42.
[27] Carrera E, Cinefra M, Petrolo M, Zappino E. Finite element analysis of structures through unified formulation. John Wiley & Sons; 2014.
[28] Carrera E, Giunta G. Refined beam theories based on a unified formulation. Int J Appl Mech 2010;2(01):117–43.
[29] de Miguel AG, Carrera E, Pagani A, Zappino E. Accurate evaluation of interlaminar stresses in composite laminates via mixed one-dimensional formulation. AIAA J 2018;56(11):4582–94.
[30] Carrera E, Giunta G, Petrolo M. Beam structures: classical and advanced theories. John Wiley & Sons; 2011.
[31] Carrera E, Petrolo M. Refined beam elements with only displacement variables and plate/shell capabilities. Meccanica 2012;47(3):537–56.
[32] Yan Y, Pagani A, Carrera E. Exact solutions for free vibration analysis of laminated, box and sandwich beams by refined layer-wise theory. Compos Struct 2017;175:28–45.

[33] Filippi M, Pagani A, Petrolo M, Colonna G, Carrera E. Static and free vibration analysis of laminated beams by refined theory based on chebyshev polynomials. Compos Struct 2015;132:1248–59.
[34] Carrera E, De Miguel AG, Pagani A. Hierarchical theories of structures based on legendre polynomial expansions with finite element applications. Int J Mech Sci 2017;120:286–300.
[35] Yan Y, Carrera E, de Miguel AG, Pagani A, Ren QW. Meshless analysis of metallic and composite beam structures by advanced hierarchical models with layer-wise capabilities. Compos Struct 2018;200:380–95.
[36] Viglietti A, Zappino E, Carrera E. Analysis of variable angle tow composites structures using variable kinematic models. Compos Part B 2019;171:272–83.
[37] Viglietti A, Zappino E, Carrera E. Free vibration analysis of variable angle-tow composite wing structures. Aerosp Sci Technol 2019;92:114–25.
[38] Pagani A, Sanchez-Majano AR. Influence of fiber misalignments on buckling performance of variable stiffness composites using layerwise models and random fields, Mech Adv Mater Struct, In press..
[39] Pagani A, Sanchez-Majano AR. Stochastic stress analysis and failure onset of variable angle tow laminates affected by spatial fibre variations. Compos Part C 2021;4:100091.
[40] Liu C, Liu B, Zhao L, Xing Y, Ma C, Li H. A differential quadrature hierarchical finite element method and its applications to vibration and bending of mindlin plates with curvilinear domains. Int J Numer Meth Eng 2017;109(2):174–97.
[41] Liu B, Liu C, Lu S, Wu Y, Xing Y, Ferreira AJM. A differential quadrature hierarchical finite element method using fekete points for triangles and tetrahedrons and its applications to structural vibration. Comput Methods Appl Mech Eng 2019;349:798–838.
[42] Carrera E, de Miguel AG, Pagani A. Extension of mitc to higher-order beam models and shear locking analysis for compact, thin-walled, and composite structures. Int J Numer Meth Eng 2017;112(13):1889–908.
[43] Xing Y, Liu B. High-accuracy differential quadrature finite element method and its application to free vibrations of thin plate with curvilinear domain. Int J Numer Meth Eng 2009;80(13):1718–42.
[44] Xing Y, Liu B, Liu G. A differential quadrature finite element method. Int J Appl Mech 2010;2(01):207–27.
[45] Varello A. Advanced higher-order one-dimensional models for fluid-structure interaction analysis. PhD thesis, Politecnico di Torino, Turin, Italy; 2013..
[46] Babuska I, Szabo BA, Katz IN. The p-version of the finite element method. SIAM J Numer Anal 1981;18(3):515–45.
[47] Daraei B, Shojaee S, Hamzehei-Javaran S. Free vibration analysis of composite laminated beams with curvilinear fibers via refined theories. Mech Adv Mater Struct, In press..